

1
2
3
4
5
6
7
8
9
10
11
12
13
14
15
16
17
18
19
20
21
22
23
24
25
26
27
28
29
30
31

Revision 1

**Characterization of ferric arsenate-sulfate compounds: Implications for
arsenic control in refractory gold processing residues**

DOGAN PAKTUNC^{1*}, JURAJ MAJZLAN², LUKÁŠ PALATINUS³, JOHN
DUTRIZAC¹, MARIANA KLEMENTOVÁ³, and GLENN POIRIER^{1,4}

¹CanmetMINING, 555 Booth St., Ottawa, ON, K1A 0G1, Canada

²Institute of Geosciences, Friedrich-Schiller University, Burgweg 11, D-07749 Jena,
Germany

³Institute of Physics of the AS CR, v.v.i., Na Slovance 2, 182 21 Prague, Czech Republic

⁴*present address:* Canadian Museum of Nature, P.O. Box 3443 Stn. “D” Ottawa, ON,
K1P 6P4, Canada

* Corresponding author dpaktunc@NRCan.gc.ca

(American Mineralogist Manuscript 4342)

32

33

ABSTRACT

34

35

36

37

38

39

40

41

42

43

44

45

46

47

48

49

50

51

52

53

54

55

56

57

58

59

60

61

62

A combination of techniques, including powder X-ray diffraction (XRD), electron microprobe analysis (EPMA), transmission electron microscopy (TEM) and X-ray absorption spectroscopy (XAFS), is used to characterize the common ferric-arsenate-sulfate compounds which could result from the pressure oxidation of refractory gold ores at elevated temperatures. Three general types of precipitate are identified; namely, arsenate-bearing basic ferric sulfate ($\text{FeSO}_4(\text{OH})$) and designated as BFS), ferric arsenate-sulfate (an extensive solid solution $\text{Fe}(\text{AsO}_4)_{0.2-0.7}(\text{SO}_4)_{0.7-0.2}(\text{OH})_{0.7-0.2}$ and designated as FAS) and hydrated ferric orthoarsenate ($\text{FeAsO}_4 \cdot 0.75\text{H}_2\text{O}$). The crystal structure of FAS is solved by precession electron-diffraction experiments. The structures of BFS and FAS are constructed from octahedral Fe^{3+} chains which are cross-linked by sulfate and arsenate tetrahedra. Extensive substitution of arsenate for sulfate occurs in both types of compound with charge neutrality being maintained of variations in the (OH) content. The XAFS spectra indicate that the local structures of both BFS and FAS are made of corner-linked single chains of FeO_6 octahedra where the chains are linked by AsO_4 or SO_4 tetrahedra forming alternating layers of FeO_6 octahedra and AsO_4 or SO_4 tetrahedra. Preliminary Toxicity Characteristics Leaching Procedure (TCLP) testing of the precipitates indicates that FAS with a molar ratio $\text{As}/(\text{As}+\text{S})$ ratio of ≤ 0.5 could be an acceptable material for disposal in a tailings impoundment whereas more As-rich FAS and BFS may require further treatment. The results for the laboratory-prepared precipitates are compared with those obtained on three residues from the processing of refractory gold ores. The major As-carrier in one of the residues is FAS, whereas As-bearing goethite and hematite are the dominant As-carriers in the other two residues. Thus, the mineralogical characteristics of the residues dictate the appropriate arsenic management and disposal options in the processing of refractory gold ores.

Keywords: arsenic, arsenate, sulfate, ferric arsenate sulfate, refractory gold, arsenic control, hydrometallurgy, autoclave residue

63

INTRODUCTION

64

65

66

67

68

69

70

71

72

73

74

75

76

77

78

79

80

In refractory gold ores, gold occurs as submicroscopic particles or in solid solution in arsenopyrite and pyrite at ppb to ppm levels; these occurrences are often referred to as “invisible gold”. Pyrite in refractory gold-sulfide deposits is often rich in As, and As contents as high as 20 wt % have been reported (Abraitis et al. 2004; Paktunc et al. 2006). Therefore, like the less abundant arsenopyrite, pyrite can be an important primary source of As in refractory gold processing circuits. Gold extraction from refractory gold ores requires a pre-treatment process such as roasting, pressure oxidation or bacterial oxidation to destroy the host sulfide so that the gold is liberated and made available for cyanide leaching. Roasting and pressure oxidation are the most commonly used pre-treatment technologies. In addition to its technical advantages, such as improved liberation of gold, pressure oxidation is preferred over roasting because of environmental concerns associated with the generation of gaseous emissions with SO₂ and As₂O₃ in the roasting process (Fleming 2010). Pressure oxidation is performed in large autoclaves commonly operating in acidic media at relatively high temperatures (i.e., 190-230 °C) to achieve complete oxidization of the sulfide minerals within a few hours. With the destruction of arsenopyrite and pyrite, significant amounts of As can be incorporated in the residues along with sulfate and ferric iron.

81

82

83

84

85

86

87

88

89

90

91

92

93

Swash and Monhemius (1994) were among the first to examine the Fe⁺³-AsO₄-SO₄ system at elevated temperatures under hydrothermal conditions. They synthesized a series of compounds including scorodite (FeAsO₄·2H₂O), basic ferric sulfate (Fe(SO₄)(OH)) and two unknown ferric arsenate and ferric arsenate-sulfate compounds, designated as Type-1 and Type-2 (Table 1). Scorodite formed at temperatures below 175 °C whereas the other compounds formed at higher temperatures which were dependent on the starting solution composition. Despite the compositional differences, the X-ray diffraction (XRD) pattern of Type-1 is similar to the ferric orthoarsenate hydrate (FeAsO₄·0.75H₂O) reported by Jakeman et al. (1991). Type-2 has a composition defined as Fe₄(AsO₄)₃(SO₄)_y(OH)_x (where x+2y=3). Similarly, Dutrizac and Jambor (2007) performed synthesis experiments in the same system to determine the compositions of the precipitates that may be analogous to those generated in industrial autoclaves. In addition to scorodite, Fe(SO₄)(OH) and two unknown compounds labelled as Phase 3 and Phase 4

94 formed. Among these, Phase 4 is a ferric arsenate with a composition of
95 $\text{Fe}_{0.96}(\text{AsO}_4)_{0.99}(\text{SO}_4)_{0.01}(\text{H}_2\text{O})_{0.54}$. Like Type-1, Phase 4 is similar to the ferric
96 orthoarsenate hydrate of Jakeman et al. (1991). Phase 3 has a wider compositional range
97 between $\text{Fe}_{0.8-1.1}(\text{AsO}_4)_{0.25}(\text{SO}_4)_{0.75}(\text{OH})_{0.75}$ and $\text{Fe}_{0.8-1.1}(\text{AsO}_4)_{0.54}(\text{SO}_4)_{0.46}(\text{OH})_{0.46}$. Based
98 on our experimental work conducted at CANMET and earlier studies conducted at
99 Imperial College (Ugarte and Monhemius 1992; Swash and Monhemius 1994), it is
100 anticipated that As and S released during the oxidation of arsenopyrite and pyrite under
101 industrial autoclave conditions would likely precipitate predominantly as a ferric
102 arsenate-sulfate phase (FAS). Despite their likelihood as the most abundant arsenic
103 compounds in autoclave residues, the characteristics and crystal structures of Phase 3 and
104 Type-2 remained unknown.

105 The objectives of this study are to characterize the common arsenical compounds
106 which would result from the pressure oxidation of refractory gold ores and to assess their
107 solubilities. In addition, three residue samples from industrial gold processing operations
108 and two samples of bukovskýite ($\text{Fe}_2(\text{AsO}_4)(\text{SO}_4)(\text{OH})\cdot 9\text{H}_2\text{O}$ (Majzlan et al. 2012a))
109 were characterized to provide a basis for comparison. Mineralogical characteristics and
110 the stability of the As species in the residues will dictate the development of appropriate
111 arsenic management and disposal options at mine sites.

112

113

METHODOLOGY

114 In order to determine the As-bearing compounds that are typically present in pressure
115 oxidation residues, a series of experiments was performed in the ferric iron, arsenate and
116 sulfate system using solutions containing reagent grade $\text{Fe}(\text{SO}_4)_{1.5}$, As_2O_5 , H_2SO_4 and
117 $\text{Fe}(\text{NO}_3)_3$. Synthesis work was performed in Parr 2-L autoclaves under hydrothermal
118 conditions at temperatures greater than ~ 100 °C with retention times varying from 1 to 5
119 hours. These experiments produced various ferric arsenate-sulfates, scorodite, ferric
120 orthoarsenate, ferric sulfate and jarosite; some of compounds were previously described
121 as Phase 3 and Phase 4 by Dutrizac and Jambor (2007). In addition, pressure oxidation
122 residue samples from three commercial gold operations, designated as POX-2, POX-9,
123 POX-14, were obtained to provide a basis for comparison with the synthesized samples.

124 The samples were characterized by a combination of techniques including powder X-
125 diffraction (XRD), electron microprobe analysis (EPMA), transmission electron
126 microscopy (TEM) and X-ray absorption spectroscopy (XAFS).

127 Powder XRD analyses were performed using a RIGAKU D/MAX 2500 rotating-
128 anode powder diffractometer with $\text{CuK}\alpha$ radiation (1.5406 Å) at 50 kV, 260 mA, a step-
129 scan of 0.02° , and a scan rate of 1° per minute in 2θ from 5 to 70° . The samples were
130 finely ground in a mortar and pestle, and packed either on Teflon covered aluminum
131 sample holders or on zero-background plates for the XRD analyses. Powder XRD
132 patterns were also collected at the bending-magnet beamline PDIFF at the synchrotron
133 light source ANKA (Angströmquelle Karlsruhe, Germany). X-rays of wavelength of
134 $0.82694(1)$ Å were selected by a double crystal Si(111) monochromator. The wavelength
135 and the zero angle of the diffractometer were determined with silicon powder (NIST
136 standard reference material 640). The sample was loaded into a 1.0 mm glass capillary
137 which was rotated about its axis during data collection. The intensity of the incoming
138 beam was monitored during data collection by an ion chamber and the measured
139 intensities of the diffracted beam were corrected for the decay and fluctuations of the
140 primary beam. The XRD patterns were collected at room temperature, over an angular
141 range of 4 to 40° in 2θ , with a step of 0.005° and counting time of 1 s per point. The
142 diffraction data were treated with a full-profile Rietveld refinement with the GSAS
143 (General Structure Analysis System) program of Larson and von Dreele (1994).

144 Electron microprobe analyses were performed by wavelength-dispersive spectrometry
145 (WDS) on carbon-coated polished sections using JEOL JXA 8900 (CANMET) and JEOL
146 8230 (Earth Sciences, University of Ottawa) microanalyzers, operated at 15 kV using a
147 probe current of 10 to 30 nA, counting times of 10 seconds and a ZAF correction. The
148 following X-ray lines and standards were used: $\text{FeK}\alpha$ (marcasite), $\text{SK}\alpha$ (marcasite) and
149 $\text{AsL}\alpha$ (synthetic GaAs).

150 Transmission electron microscopy (TEM) examination of the samples, including
151 structural determinations, was conducted on a Philips CM120 microscope with a LaB_6
152 cathode operating at 120 kV. The microscope is equipped with a DigiStar (NanoMegas)
153 precession device for application of the precession electron diffraction (PED) and with a
154 CCD Camera Olympus SIS Veleta with a 14-bit dynamical range. Precession electron

155 diffraction was used to suppress the dynamical diffraction effects to as large an extent as
156 possible. Small, homogeneous crystals were selected for the diffraction experiment. The
157 crystals were not oriented along a special zone axis prior to the data collection but were
158 intentionally left in a random orientation. During the data collection the crystal was tilted
159 in steps of 1° around the main tilt axis of the sample holder, and at each tilt a diffraction
160 pattern was recorded. This experimental method dubbed “electron diffraction
161 tomography” and pioneered by Kolb and coworkers (Mugnaioli et al., 2009) allows a
162 collection of 3-dimensional electron diffraction data set and subsequent *ab initio* solution
163 of crystal structures from electron diffraction data. The data were processed using the
164 computer programs PETS (Palatinus, 2011) and Jana2006 (Petříček et al., 2006), to yield
165 the unit cell parameters and integrated reflection intensities. The crystal structures were
166 solved *ab initio* using the computer program Superflip (Palatinus and Chapuis, 2007),
167 and refined with Jana2006 (Petříček et al., 2006).

168 XAFS spectroscopy measurements were made at the Pacific Northwest Consortium’s
169 (PNC-CAT) bending magnet beam line of the Advanced Photon Source. Samples were
170 packed in Teflon sample holders after mixing with boron nitride to achieve a sample
171 thickness of about one absorption length. Each sample was scanned 5 to 8 times at room
172 temperature in both the transmission and fluorescence modes. Data reduction and
173 analysis were accomplished by ATHENA and ARTEMIS (Ravel and Newville 2005)
174 with data analysis considering the theoretical phase and amplitude functions generated in
175 FEFF6 (Zabinsky et al. 1993).

176 The samples were subjected to the Toxicity Characteristics Leaching Procedure
177 (TCLP) test (USEPA 1992). Due to the homogenous and fine-grained nature of the
178 precipitates, only 5 g samples of the precipitates were contacted for 20 hours at room
179 temperature by 100 mL of deionised water buffered at pH 5. Prior to the tests, the
180 samples were water-washed to remove any possible remaining soluble secondary salts
181 and dried at 100°C. The residue materials following the TCLP tests were filtered through
182 0.1 µm filters and the solutions were analysed for As, Fe and S by ICP-AES (Varian,
183 Vista RL) and ICP-MS (Thermo Scientific X-series 2) techniques.

184
185

186

RESULTS AND DISCUSSION

187 Long-range structures and chemical compositions

188 The chemical composition of the precipitates formed from solutions with initial Fe/As
189 molar ratios ≥ 1.6 is highly variable from 29.0 to 33.3 wt % Fe, 0.1 to 43.2 wt % AsO_4
190 and 15.6 to 56.6 wt % SO_4 . In terms of the Fe, AsO_4 and SO_4 molar contents, the
191 variation is essentially continuous as illustrated in Figure 1. The composition of the
192 samples projects from the point with a Fe: SO_4 ratio of 1 to $\text{Fe}(\text{AsO}_4)_{0.5}(\text{SO}_4)_{0.5}$, but
193 deviates towards $\text{Fe}_{1.5}\text{AsO}_4$ as the AsO_4 content increases and the SO_4 content decreases.
194 This trend requires that OH initially decreases from 1 to 0.5 in unison with the decrease
195 in SO_4 , and this substitution can be written as $\text{SO}_4^{2-} + \text{OH}^- = \text{AsO}_4^{3-}$. In this case, the
196 change in the formula would be from $\text{Fe}(\text{SO}_4)(\text{OH})$ to $\text{Fe}(\text{AsO}_4)_{0.5}(\text{SO}_4)_{0.5}(\text{OH})_{0.5}$. For the
197 compositions in which AsO_4 dominates over SO_4 , the formulae change between
198 $\text{Fe}(\text{AsO}_4)_{0.5}(\text{SO}_4)_{0.5}(\text{OH})_{0.5}$ and $\text{Fe}_{1.5}\text{AsO}_4(\text{OH})_{1.5}$. This substitution can be formally
199 written as $\text{SO}_4^{2-} = \text{Fe}^{3+} + \text{AsO}_4^{3-} + 2\text{OH}^-$. Based on the powder XRD patterns (Fig. 2),
200 the precipitates were grouped as Type-2, Phase 3 and Phase 5. In the following text, we
201 describe the structures of all the identified phases and the variations thereof with the
202 observed AsO_4 - SO_4 substitutions. We begin with the sulfur-rich phases and proceed
203 toward the most arsenic-rich one, as shown in Figure 1.

204 **Jarosite.** Jarosite, nominally $\text{KFe}_3(\text{SO}_4)_2(\text{OH})_6$, has a dense heteropolyhedral
205 structure with octahedral kagomé sheets, sulfate tetrahedra, and monovalent cations (K^+ ,
206 but several other ions including H_3O^+) in twelve-fold coordination (Fig. 3a). Because of
207 its relatively dense atomic arrangement, the AsO_4 - SO_4 substitution is limited and the
208 maximum was reported to be 17 % $\text{AsO}_4/(\text{AsO}_4+\text{SO}_4)$ (Paktunc and Dutrizac 2003).
209 These authors investigated the incorporation of As^{5+} in the jarosite structure in detail and
210 their analyses and conclusions will not be repeated here.

211 **Basic ferric sulfate (BFS).** Another nominally arsenic-free phase with limited AsO_4 -
212 SO_4 substitution is $\text{Fe}(\text{SO}_4)(\text{OH})$, hereafter referred to as basic ferric sulfate (BFS). The
213 structure of this phase was solved by Johansson (1962) and was shown to be in the
214 orthorhombic space group *Pnma*. Ventrucci et al. (2005) investigated the order-disorder
215 nature of the structure of BFS and showed that the orthorhombic phase of Johansson
216 (1962) is one of two maximum-degree-of-order (MDO) phases. The other MDO

217 Fe(SO₄)(OH) phase is monoclinic, space group *P2₁/c*. Small changes in the stacking
218 order between the two MDO phases results in small modifications in the powder XRD
219 patterns. These changes, especially visible in the intensities of selected peaks, can be
220 qualitatively traced in our XRD data. Structures of both MDO Fe(SO₄)(OH) phases are
221 heteropolyhedral frameworks. In contrast to jarosite, the Fe³⁺ octahedra in Fe(SO₄)(OH)
222 are arranged in chains and cross-linked by the tetrahedral units (Fig. 3b). A peculiar
223 change in lattice parameters upon substitution of AsO₄ for SO₄ can be observed (Fig. 4).
224 With the addition of a small amount of AsO₄, the unit-cell volume initially decreases
225 despite the fact that the AsO₄ tetrahedron is significantly larger than the SO₄ tetrahedron.
226 Only upon further insertion of AsO₄ into the structure does the unit-cell volume begin to
227 expand. A closer inspection of the lattice parameters (in the orthorhombic phase setting
228 *Pnma*) reveals the non-linear change of *a* and near linear expansion of *b* and *c* (Fig. 4b).
229 This observation is interesting because the octahedral chains extend in the direction of the
230 *a* axis. Tetrahedra are bridging FeO octahedra along the chains and the shared oxygen
231 atoms are perfectly aligned with the oxygen atoms linking the octahedra; therefore,
232 substitution of smaller sulfate by the larger arsenate (e.g. S-O=1.47 Å vs. As-O=1.68 Å)
233 would translate to the largest increases along the *a* axis. Three adjacent octahedral chains
234 are cross-linked or anchored by the tetrahedra; therefore, expansions along the *b* and *c*
235 axes would be restricted. It seems that with a small amount of AsO₄, the chains are
236 allowed to relax and actually contract. The expansion of the unit cell (i.e., the octahedral
237 chains) begins only with higher amounts of AsO₄, at 2 % AsO₄/(AsO₄+SO₄). It appears
238 that BFS is able to accommodate up to about 10 wt % AsO₄, which corresponds to the
239 *X*_{As} mole fraction of 0.12. Interestingly, this is similar to the limit of AsO₄-SO₄
240 substitution in jarosite (Paktunc and Dutrizac 2003).

241 Our powder XRD data suggest that the BFS samples contain a minor amount of
242 hydronium jarosite. In addition, the BFS samples with the highest As content contain
243 Phase 3, which is chemically and structurally related to BFS and is described in detail
244 below.

245 **Ferric arsenate sulfate (FAS).** Phase 3 which spans most of the mixed SO₄-AsO₄
246 compositions (Fig. 1) is a ferric arsenate-sulfate (FAS). Structure of this phase was not
247 known previously, but the powder XRD data bear a remarkable similarity to the

248 monoclinic $\text{Fe}(\text{SO}_4)(\text{OH})$. Despite this similarity, the structure solution of FAS turned out
249 to be a difficult problem.

250 Early attempts to index the synchrotron powder XRD data failed because of the small
251 amount of impurities in the samples. TEM examinations indicated that FAS is the major
252 phase and occurs as isometric or blocky crystals, often twinned (Fig. 5). Energy-
253 dispersive X-ray microanalyses indicate that the crystals have a variable S:As ratio in the
254 range of 0.7-1. The electron diffraction tomography data were collected on a small crystal
255 with dimensions 130x180 nanometres. In total, 118 diffraction patterns with exposure
256 time 2 s were collected. The data analysis revealed that the FAS is triclinic (pseudo-
257 orthorhombic), with approximate lattice parameters $a=5.42 \text{ \AA}$, $b=5.44 \text{ \AA}$, $c=13.58 \text{ \AA}$, and
258 $\alpha=89.21^\circ$, $\beta=89.68^\circ$, $\gamma=87.89^\circ$, space group $I-1$. Just as BFS, the structure of FAS is
259 constructed from octahedral Fe^{3+} chains which are cross-linked by sulfate and arsenate
260 tetrahedra (Fig. 6). The atomic positions of the structure as refined against the electron
261 diffraction data are given in Table 2. It should be emphasized that this structure is only
262 approximate, as the refinement does not take into account the dynamical scattering
263 effects. However, the experience with the refinement from precession electron diffraction
264 data shows that the errors in the refined atomic positions often range around 0.1-0.2 \AA ,
265 and very rarely exceed 0.5 \AA (Gorelik *et al.* 2011).

266 The lattice parameters refined from the X-ray powder diffraction data are $a=5.1663$,
267 $b=5.1892$, $c=12.917 \text{ \AA}$ and $\alpha=89.000^\circ$, $\beta=89.645^\circ$, $\gamma=87.868^\circ$. These refined parameters
268 agree well with those determined from electron diffraction data supporting the triclinic
269 symmetry with the exception of an overall scaling factor of ~ 1.05 , resulting from
270 imperfect calibration of the electron diffraction patterns.

271 The FAS phase precipitates from solutions with initial Fe/As molar concentrations
272 ≥ 1.5 at temperatures between 180 and 220 $^\circ\text{C}$. It is the most abundant precipitate with X_{As}
273 mole fractions varying from 0.26 to 0.63. The lower end of this range seems to
274 correspond to higher synthesis temperatures.

275 Profile fitting of the in-house and synchrotron powder XRD data obtained from the
276 samples with variable X_{As} mole fractions shows an intriguing trend (Fig. 4, Table 3). As
277 was the situation for the BFS, the unit-cell volume does not change linearly with
278 increasing amounts of AsO_4 in the structure. Within the scatter of the data, the unit-cell

279 volume increases linearly up to $X_{As} \sim 0.55$, but then levels off for the most As-rich
280 compositions. These changes are most likely related to the capability of the octahedra
281 within the chains to rotate and adjust for the attachment of the sulfate or arsenate
282 tetrahedra.

283 Type-2 synthesized by Swash and Monhemius (1994) with the X_{As} mole fraction of
284 0.75 has an XRD pattern similar to that of FAS, and this indicates that they are essentially
285 the same compound (Fig. 2). Electron microprobe analyses of the material synthesized by
286 Swash and Monhemius (1994) revealed that Type-2 is not homogeneous. The grains
287 showing hedge-hog type morphology display zoning with respect to As and S (Fig. 7a).
288 Some of the grains have margins with increased As and decreased S contents. In addition,
289 the X-ray maps show sulfur-deficient rosettes within the grains indicating a ferric
290 arsenate phase exsolved from the compound (Fig. 7b). Electron microprobe analyses
291 indicate that the exsolved phase has X_{As} mole fractions varying from 0.77 to 0.96 with an
292 average value of 0.90 ± 0.05 ; however, it is possible that this exsolved phase is nearly
293 sulfate-free. Furthermore, because of the small size, it is likely that some of the S counts
294 in the microanalyses originate from the host phase. The X_{As} mole fraction of the main
295 phase is 0.69 ± 0.05 . The structural formula of the dominant phase is determined to be
296 $Fe_{1.1-1.3}(As_{0.6-0.8}S_{0.2-0.4}O_4)(OH)_{0.2-0.4}$. It appears that this composition represents an end-
297 member of FAS with the highest X_{As} fraction in the structure. The structural formula of
298 the exsolved phase is $Fe_{1.1-1.5}(As_{0.8-1.0}S_{0.0-0.2}O_4)(OH)_{0.0-0.2}$. In summary, the composition of
299 FAS can be defined as $Fe(AsO_4)_{0.2-0.7}(SO_4)_{0.7-0.2}(OH)_{0.7-0.2}$ where $AsO_4 + SO_4 = 1$.

300 **Scorodite.** Scorodite, nominally $FeAsO_4 \cdot 2H_2O$, is another heteropolyhedral network
301 among the studied phases. The structure consists of monomers of $FeO_4(H_2O)_6$ polyhedra
302 which attach via the oxygen ligands to the four neighboring AsO_4 tetrahedra (Fig.3c).
303 Little SO_4 can be incorporated into the scorodite structure and from the limited data
304 acquired herein, it seems that the unit cell contracts monotonically with increasing SO_4
305 substitution (Table 3).

306 **Ferric orthoarsenate hydrate.** In our synthesis experiments, $FeAsO_4 \cdot 0.75H_2O$ is the
307 phase with the least amount of SO_4 . The structure of this phase was reported by Jakeman
308 et al. (1991). The structure is built by kinked tetramers of edge-sharing of $Fe(O, H_2O)_6$
309 octahedra (Fig.3d). The tetramers are interlinked by the AsO_4 tetrahedra in a tightly

310 knitted heteropolyhedral framework which probably does not leave much room for the
311 substitution of the smaller SO_4 group. This phase forms when the Fe/As molar ratio of the
312 initial solution is low (i.e., near 1) and at synthesis temperatures of 180°C and greater. At
313 lower temperatures, between 150 and 175°C , the precipitate is scorodite.

314

315 **Short-range structures**

316 The k^3 -weighted As K-edge spectra of BFS and FAS samples are broadly similar
317 (Fig. 8a). The k^3 -weighted Fe K-edge XAFS spectra also display similarities (Fig. 8b).
318 The changes in the spectra point to the progressive variation of the X_{As} mole fractions in
319 the precipitates. This indicates that the local structures around the As and Fe atoms in
320 BFS and FAS are similar, and this confirms the continuity in the long-range structures
321 discussed earlier. The gradual changes in the oscillation features of the Fe K-edge XAFS
322 spectra reflect the differences in the number of As and S atoms surrounding the central Fe
323 atoms. For instance, the gradual development of humps on the low k sides of the
324 oscillation features at $\sim 4, 6$ and 8 \AA^{-1} in samples with X_{As} mole fractions ≤ 0.35 suggests
325 the influence of S. The changes in the As K-edge XAFS spectra are not as apparent
326 suggesting that the local As environment is not significantly affected by the changes in
327 the X_{As} mole fraction. Instead, it appears that Fe is the closest neighbour surrounding the
328 AsO_4 tetrahedra in both compounds. Considering these similarities and the gradual
329 changes in the spectral features, the XAFS fitting was intended to test the similarity of the
330 compounds to the $\text{Fe}(\text{SO}_4)(\text{OH})$ structure in terms of local structures around the As and
331 Fe atoms. In the $\text{Fe}(\text{SO}_4)(\text{OH})$ structure, a central Fe atom is surrounded by four S atoms
332 at 3.31 \AA and two Fe atoms at 3.67 \AA , whereas a central S atom, which is assumed to be
333 substituted by As in this case, is surrounded by four Fe atoms at 3.31 \AA and four S atoms
334 at 4.09 \AA .

335 Local structural parameters determined by As and Fe XAFS fitting for the BFS and
336 FAS compounds are given in Tables 4 and 5, and the fits are shown in Figure 8. By
337 limiting the number of variables through constraining the coordination numbers from the
338 crystal structure, it was possible to include up to 4 coordination shells in fitting. This
339 allowed an independent assessment of the interatomic distances around As and Fe atoms
340 and the changes due to arsenate-for-sulfate substitution. The As-O radial distances are

341 relatively uniform at 1.68 ± 0.01 and 1.69 ± 0.01 Å. Beyond the oxygen shell, spectral
342 features at 3.36 ± 0.02 (3.34-3.39), 3.73 ± 0.02 (3.70-3.76) and 4.03 ± 0.03 (3.99-4.07) Å
343 correspond to Fe, S and As atoms, respectively. As expected, the variations in the As-Fe,
344 As-S and As-As distances do not appear to be influenced by the changes in the X_{As} mole
345 fraction in the structures. The As-S radial distances are shorter than those of the As-As
346 due to smaller size of the sulfate tetrahedra. Fit quality was improved with the inclusion
347 of the multiple scattering paths, As-O1-O2, As-O1-As-O2 and As-O1-As-O1 derived
348 from FEFF calculations (Ankudinov et al. 1998) based on the crystal structure of
349 scorodite from Kitahama et al. (1975).

350 Fitting of the Fe K-edge XAFS spectrum of the BFS samples resulted in Fe-O
351 distances of 1.99 ± 0.01 - 2.00 ± 0.01 Å in octahedral coordination and Fe-S distances of
352 3.34 ± 0.03 - 3.38 ± 0.03 Å (Table 5). In contrast, the FAS samples have slightly shorter
353 Fe-O distances at 1.96 ± 0.01 and 1.97 ± 0.01 Å. Because of the similarity of the Fe-As and
354 Fe-S interatomic distances, simulations of the second shell were performed with As for
355 the FAS samples which resulted in Fe-As distances of 3.31 ± 0.02 - 3.34 ± 0.02 Å. These
356 are comparable to the As-Fe distances of 3.34 ± 0.02 - 3.39 ± 0.03 Å from the As-XAFS
357 and the nominal FAS distances varying from 3.25 to 3.38 Å (3.33 ± 0.05 Å). Constraining
358 the coordination numbers to their structural values made it possible to include two Fe
359 shells in the simulations. The first Fe shell with a coordination number of 2 is at
360 3.69 ± 0.03 - 3.71 ± 0.05 Å for the BFS and 3.62 ± 0.10 - 3.68 ± 0.04 Å for the FAS samples,
361 representing corner-linked FeO_6 octahedra along the octahedral chains. The second Fe
362 shell with a coordination number of 8 is at 5.10 ± 0.03 - 5.12 ± 0.02 Å for the BFS and
363 5.14 ± 0.04 - 5.18 ± 0.04 Å for the FAS samples representing corner-linked FeO_6 dimers in
364 the four adjacent octahedral chains. These Fe-Fe radial distances are comparable to the
365 Fe-Fe distances of 3.67 and 5.14 Å of the $Fe(SO_4)(OH)$ structure (Johansson 1962), and
366 3.76 and 5.17 Å of the FAS structure (this study). The increased Fe-Fe₂ distances of the
367 FAS samples indicate that the arsenate-for-sulfate substitution causes increases in
368 distance between the octahedral chains which reflect the increases along *a* and *b*.

369 In summary, the XAFS-derived interatomic distances are comparable to their
370 counterparts from the crystal structures of FAS and BFS. The average S-O distances of
371 1.457 Å in $Fe(SO_4)(OH)$ and 1.473 Å in sulfate minerals (Hawthorne et al. 2000) are

372 shorter by about 0.22 Å from the measured As-O distance of 1.68 Å. It is possible that the
373 observed differences between the As-As and As-S distances, ranging from 0.29±0.06 to
374 0.32±0.07 Å, are reflecting this difference. In addition, substitution of sulfate ions by the
375 larger arsenate ions would cause the Fe-Fe distance to become greater, lengthening the
376 iron chains and widening the distance between the octahedral chains. This would explain
377 the gradual shifts to lower 2θ or wider *d*-spacings and the enlargement of the unit-cell
378 volume with increased arsenate substitution.

379

380 **Leachability**

381 TCLP testing was used to make a preliminary assessment of the environmental
382 stability of the BFS and FAS precipitates. Materials that produce effluents with As
383 concentrations exceeding the Canadian metal-mine effluents limit of 0.5 mg/L
384 (Government of Canada 2002) could be considered unacceptable for safe disposal in the
385 environment, and even materials which pass this short-term test often require testing for
386 longer times at various pH values and under a range of oxidation/reduction conditions.
387 TCLP testing of the BFS with an X_{As} mole fraction of 0.08 resulted in an As
388 concentration of 16.2 mg/L in the leachate. The FAS samples produced As concentrations
389 that varied between 0.06 and 0.88 mg/L. The upper end of this range is represented by the
390 sample with the highest X_{As} molar fraction (i.e., 0.62). Swash and Monhemius (1994)
391 reported that Type-2 with an X_{As} mole fraction of 0.75 produced a similar As
392 concentration (i.e., 0.8 mg/L) in the TCLP leachate at pH 5. Some of the FAS samples
393 contain trace to minor amounts of BFS, as evidenced by the presence of overlapping
394 peaks at 2θ values of ~26.5° and 27.5° which appear as asymmetric and broadened peaks.
395 The BFS samples containing minor amounts of FAS have leachate As concentrations
396 between 0.46 and 2.26 mg/L. Arsenic concentrations in the leachates of the FAS samples
397 increase exponentially with a decrease in the leachate Fe concentration (Fig. 9), although
398 all the As concentrations are less than 1 mg/L. This is with the exception of the samples
399 containing minor amounts of BFS. In contrast, the As and Fe concentrations in the
400 leachates of BFS and those containing both compounds display a positive correlation.
401 Leachate S concentrations are variable from 55.6 to 252.7 mg/L in the samples containing
402 BFS and less than 1 to 39.6 mg/L in the FAS samples, forming a trend of increasing Fe

403 and S concentrations from both types of precipitates (Fig. 9). The highest releases of As,
404 Fe and S are from BFS. Leachate Fe concentrations of 13 to 259 mg/L released from BFS
405 and the FAS samples containing BFS are unusually high for solutions at the TCLP test
406 value of pH 4.5.

407 The FAS samples with X_{As} mole fractions of 0.40, 0.42 and 0.52 gave the lowest As
408 concentrations in the leachates (i.e., 0.063-0.069 mg/L) and also yielded molar Fe/As
409 ratios that are greater than 20. These samples contain trace amounts of BFS. For
410 precipitates with molar Fe/As+S ratios between 0.002 and 0.572, the releases of Fe, As
411 and S from both the FAS and BFS precipitates are non-stoichiometric. The highest ratio
412 is from a BFS sample indicating that dissolution of BFS releases about twice as much As
413 and S as Fe. With the exception of the samples containing minor to trace BFS, the molar
414 Fe/As+S ratios of the TCLP extracts of the FAS samples are less than 0.008 indicating
415 that very little iron is released in comparison to the combined As and S releases from the
416 dissolution of FAS. In consideration of the crystal structure of BFS, the non-
417 stoichiometric dissolution behaviour can be explained by the precipitation of a ferric
418 oxyhydroxide phase or by the preferential release of SO_4 leaving behind chains of FeO_6
419 octahedra.

420

421 **Implications for the disposal of gold processing residues**

422 Fine grained residue samples from three autoclaves treating refractory gold ores were
423 obtained. In terms of bulk chemical compositions, the sample designated as POX-2
424 analyzed 22.7% Fe, 5.42% As and 3.90% SO_4 . The POX-9 sample analyzed 12.9% Fe,
425 2.39% As and 1.40% SO_4 ; the analysis of the POX-14 sample was 20.0% Fe, 4.01% As
426 and 3.50% SO_4 . Electron microprobe analyses of the heterogeneous oxidation residues
427 indicate that the arsenic carrier in the POX-2 sample is a FAS compound (Fig. 10). The
428 POX-9 sample has jarosite, hematite and goethite as the main As carriers. The jarosite
429 has significant amount of Al and contains between 0.5 and 8.6 wt % As_2O_5 . Hematite has
430 3.6 to 6.1 wt % As_2O_5 whereas goethite contains much higher As concentrations, in the
431 7.9 to 23.5 wt % range. Goethite, with As_2O_5 concentrations in the 0.1 to 14.9 wt %
432 range, is the dominant As carrier in the POX-14 sample. The compositional similarity of
433 the POX-2 residues to the As-rich members of Phase 3 or Type-2 is apparent on the Fe-

434 AsO₄-SO₄ plot (Fig. 10). Spherical ferric arsenate-sulfate grains from the Red Lake
435 autoclave (McCredie et al. 1998) have a similar composition. The POX-14 data cluster
436 near the Fe³⁺ corner along the Fe-AsO₄ join in agreement with the compositions of As-
437 adsorbed goethite and hematite. The arsenic carriers in the POX-9 residue plot with those
438 of POX-14 and are close to the Fe³⁺ corner and near the mid point along the Fe-SO₄ join
439 close to the theoretical jarosite composition. In terms of contained As, these residues are
440 similar to the synthetic arsenical jarosites reported by Paktunc and Dutrizac (2003).

441 In agreement with their chemical compositions, analysis of the As-XAFS spectra of
442 the POX-2 and POX-14 residue sample (Fig. 11) yielded local structural parameters that
443 are similar to those of FAS and goethite, respectively (Table 6). POX-9 has an optimized
444 iron coordination number of 2 but the As-Fe radial distance is rather long at 3.40±0.10 Å
445 in comparison to the 3.24-3.32 Å distances for goethite (Foster et al. 1998; Sherman and
446 Randall 2003; Paktunc et al. 2004; 2008), 3.25-3.26 Å for jarosite (Paktunc and Dutrizac
447 2003), and 3.24-3.35 Å for hematite (Sherman and Randall 2003). However, considering
448 the large uncertainty associated with the measured As-Fe distance for POX-9 and the
449 number of As carriers in the sample, the calculated “average” As-Fe distance is not
450 unreasonable.

451 Minerals in the Fe-AsO₄-SO₄ system are also shown on the Fe-AsO₄-SO₄ plot (Fig.
452 10). The minerals are essentially restricted to near Fe/anion ratios of 1 and 1.5.
453 Kaatialaite with a Fe/As molar ratio of 1/3 is the exception but this is a very rare mineral
454 found only in extremely acidic environments. Other than scorodite, jarosite, hematite and
455 goethite, the compounds that form during pressure oxidation do not have natural analogs.
456 There are three ferric arsenate-sulfate minerals, bukovskýite
457 (Fe(AsO₄)_{0.5}(SO₄)_{0.5}(OH)_{0.5}·4.5H₂O), sarmientite (Fe(AsO₄)_{0.5}(SO₄)_{0.5}(OH)_{0.5}·2.5H₂O)
458 and zykaite (Fe₄(AsO₄)₃(SO₄)(OH)·15H₂O). The exsolved ferric arsenate phase present in
459 the FAS sample with the highest As content is similar to ferrisymplectite
460 (Fe₃(AsO₄)₂(OH)₃·5H₂O in terms of the Fe/As ratio. Ferrisymplectite is an amorphous
461 ferric arsenate supposedly resulting from the oxidation of symplectite, but little is known
462 about this compound and its existence as a valid mineral species may be questionable.
463 Bukovskýite and sarmientite could be considered as hydrated natural analogs of FAS
464 with equal numbers of AsO₄ and SO₄ molecules in the structure. Along with zykaite and

465 kaatialaite, these are uncommon arsenate minerals, occurring as alteration products of
466 scorodite and arsenopyrite in several mine waste sites. The As-XAFS spectra of two
467 bukovskýite specimens from Kutná Hora (Czech Republic) and the Ketzá River mine in
468 Yukon (Canada) display similarities to those of FAS (Fig. 11). Local structural
469 parameters of bukovskýite determined by As-XAFS are four O at 1.69 ± 0.01 Å, four Fe at
470 3.33 ± 0.03 Å and two As at 3.97 ± 0.07 Å (Table 6). Fitting of the Fe-XAFS spectra (Fig.
471 11b) resulted in six O at 1.99 ± 0.01 Å, two As at 3.35 ± 0.02 Å and one Fe at 3.61 ± 0.03 Å
472 and one Fe at 5.09 ± 0.05 Å (Table 7). These independently determined local structures are
473 reasonable in consideration of the crystal structure of bukovskýite (Majzlan et al. 2012a)
474 and they are broadly similar to the local structures of FAS, indicating that bukovskýite
475 and FAS have similar local structures around As and Fe in the sense that arsenate
476 tetrahedra link octahedral “chains” which are only dimers in bukovskýite.

477 Most of the FAS samples have TCLP As concentrations that are less than the
478 Canadian metal-mine effluent limit of 0.5 mg/L (Government of Canada 2002)
479 suggesting that FAS could meet the current regulatory guideline for mine effluents at pH
480 5. The precipitates having X_{As} mole fractions between 0.4 and 0.5 could even meet
481 stricter mine effluent limit of 0.2 mg/L imposed by the Provincial Government of Québec
482 for new operations (Gouvernement du Québec 2005). In contrast, the BFS with an X_{As}
483 mole fraction of 0.08 yields 16.2 mg/L As in the TCLP leachate. This is only a
484 preliminary assessment, however, as these short-term tests may not represent the
485 solubility or near equilibrium conditions. Type-2 which has the highest As content and an
486 exsolved ferric arsenate compound, has As leachate values of less <0.5 to 7.3 mg/L,
487 determined at pH values of 3, 5, 7 and 10 by Swash and Monhemius (1994). This
488 suggests that As control by FAS precipitation would be acceptable only over the limited
489 pH range from 3 to 5. Nevertheless, these preliminary assessment results for FAS are
490 promising in that they are comparable to the solubility levels of scorodite (Krause and
491 Ettel 1989; Paktunc and Bruggeman 2010; Majzlan et al. 2012b).

492 Limited leaching tests indicate that the basic orthoarsenate hydrate (i.e., Phase 4 of
493 Dutrizac and Jambor 2007 and the Type-1 compounds of Swash and Monhemius 1994)
494 would not be suitable for disposal. Similarly, BFS would be an unwanted compound
495 because of its high solubility which would result in the release of much of the contained

496 As. In addition to environmental concerns, the formation of $\text{Fe}(\text{SO}_4)(\text{OH})$ can cause
497 problems during subsequent cyanidation and impact on the economics of the process by
498 causing excessive lime consumption during cyanidation and potentially exposing the
499 plant workers to hazardous HCN gas as pointed out by Fleming (2010). According to
500 Fleming et al. (2008), the autoclave temperatures should be around 190°C for the
501 optimum recovery of gold from the refractory Kittila ore. Higher temperatures, around
502 $210\text{-}230^\circ\text{C}$, promote the formation of $\text{Fe}(\text{SO}_4)(\text{OH})$. Accordingly, As control practices at
503 mine sites could aim to optimize the conditions for the formation of FAS at the lower end
504 of the temperature range ($185\text{-}225^\circ\text{C}$) during pressure oxidation, without compromising
505 gold recoveries.

506

507

ACKNOWLEDGEMENTS

508 Derek Smith, Al Kuiper and Ceferino Soriano helped with the laboratory and
509 analytical work at CanmetMINING. The XAFS measurements were performed at the
510 PNC-CAT beamline at the Advanced Photon Source (APS) under a General User
511 Proposal to the senior author and a Partner User Proposal supported by the Natural
512 Sciences and Engineering Research Council of Canada through a major facilities access
513 grant. Research at the PNC-CAT beamline of APS, Argonne National Laboratory is
514 supported by the US Department of Energy under Contracts W-31-109-Eng-38 (APS)
515 and DE-FG03-97ER45628 (PNC-CAT). Robert Gordon helped with the experiments at
516 the beamline. Peter Swash's earlier collaboration in terms of providing several samples
517 including Type-2 specimen is acknowledged. We acknowledge the ANKA
518 Angströmquelle Karlsruhe for the provision of the beamtime at the PDIFF beamline and
519 thank S. Doyle for the help during the measurements. Parts of this study were financially
520 supported by the Deutsche Forschungsgemeinschaft, grant no. MA 3927/16-1. We thank
521 associate editor, Richard Wilkin and the journal referees, Michael Schindler and an
522 anonymous reviewer for their efforts.

523

524

REFERENCES CITED

- 525 Abraitis, P.K., Patrick R.A.D., and Vaughan D.J. (2004) Variations in the compositional,
526 textural and electrical properties of natural pyrite: a review. *International Journal of*
527 *Mineral Processing*, 74, 41-59.
- 528 Ankudinov, A.L., Ravel, B., Rehr, J.J., and Conradson S.D. (1998) Real space multiple
529 scattering calculation and interpretation of X-ray absorption near edge structure.
530 *Physical Reviews*, B 58, 7565.
- 531 Dutrizac, J.E. and Jambor, J.L. (2007) Characterization of the iron arsenate-sulfate
532 compounds precipitated at elevated temperatures. *Hydrometallurgy*, 86, 147-163.
- 533 Fleming, C.A. (2010) Basic ferric sulfate – A potential killer in the processing of
534 refractory gold concentrates by pressure oxidation. *Minerals and Metallurgical*
535 *Processing*, 27, 81-88.
- 536 Fleming, C., Geldart, J., Blatter, P., Cousin, P., and Robitaille, J. (2008) Flowsheet
537 development for Agnico Eagle’s refractory gold Kittila project in Finland.
538 *Proceedings 6th International Symposium of Hydrometallurgy 2008*, Ed. Young,
539 C.A., Taylor P.R., Anderson C.G. and Choi Y. Society for Mining, Metallurgy and
540 Exploration Inc., Littleton, CO 404-413.
- 541 Foster, A., Brown, G., Tingle, T.N., and Parks, G.A. (1998) Quantitative arsenic
542 speciation in mine tailings using X-ray absorption spectroscopy. *American*
543 *Mineralogist*, 83, 553–568.
- 544 Gorelik, T.E., Stewart, A.A., and Kolb, U. (2011) Structure solution with automated
545 electron diffraction tomography data: different instrumental approaches. *Journal of*
546 *Microscopy*, 244, 325-331
- 547 Government of Canada (2002) Metal Mining Effluent Regulations. *Canada Gazette Part*
548 *II*, v. 136, No. 13, pp.1412-1462.
- 549 Gouvernement du Québec (2005) Directive 019 sur l’industrie minière – avril 2005.
550 Ministère du Développement durable, de l’Environnement et des Parcs, Direction
551 des politiques de l’eau service des eaux industrielles, Envirodoq : ENV/2005/0120.
- 552 Hawthorne, F.C. (1976) The hydrogen positions in scorodite. *Acta Crystallographica*,
553 B32, 2891-2892.
- 554 Hawthorne, F.C., Krivovichev, S.V., and Burns, P.C. (2000) The crystal chemistry of
555 sulfate minerals. In *Sulfate Minerals: Crystallography, Geochemistry, and*

- 556 Environmental Significance (C.N. Alpers, J.L. Jambor and D.K. Nordstrom, eds.).
557 Rev. Mineral. Geochem. 40, 1-112.
- 558 Jakeman, R.J.B., Kwiecien, M.J., Reiff, W.M., Cheetham, A.K., and Torardi, C.C. (1991)
559 A new ferric orthoarsenate hydrate: Structure and magnetic ordering of FeAsO_4
560 $\cdot\frac{3}{4}\text{H}_2\text{O}$. Inorganic Chemistry, 30, 2806-2811.
- 561 Johansson, G. (1962) On the crystal structures of FeOHSO_4 and InOHSO_4 . Acta Chemica
562 Scandinavica, 16, 1234-1244.
- 563 Kitahama, K., Kiriya, R., and Baba, Y. (1975) Refinement of the crystal structure of
564 scorodite. Acta Crystallographica, B31, 322-324.
- 565 Krause, E. and Ettel, V.A., 1989. Solubilities and stabilities of ferric arsenate compounds.
566 Hydrometallurgy, 22, 311-337.
- 567 Larson, A.C. and von Dreele, R.B. (1994) GSAS. General Structure Analysis System.
568 LANSCE, MS-H805, Los Alamos, New Mexico.
- 569 Majzlan, J., Lazic, B., Armbruster, T., Johnson, M.B., White, M.A., Fisher, R.A., Plášil,
570 J., Loun, J., Škoda, R., and Novák, M. (2012a) Crystal structure, thermodynamic
571 properties, and paragenesis of bukovskýite, $\text{Fe}_2(\text{AsO}_4)(\text{SO}_4)(\text{OH})\cdot 9\text{H}_2\text{O}$. Journal of
572 Mineralogical and Petrological Sciences, 107, 133-148.
- 573 Majzlan, J., Drahota, P., Filippi, M., Grevel, K.-D., Kahl, W.-A., Plášil, J., Woodfield,
574 B.F., and Boerio-Goates, J. (2012b) Thermodynamic properties of scorodite and
575 parascorodite ($\text{FeAsO}_4\cdot 2\text{H}_2\text{O}$), kaňkite ($\text{FeAsO}_4\cdot 3.5\text{H}_2\text{O}$), and FeAsO_4 .
576 Hydrometallurgy, 117-118, 47-56.
- 577 Manceau, A., Lanson, M., and Geoffroy, N. (2007) Natural speciation of Ni, Zn, Ba, and
578 As in ferromanganese coatings on quartz using X-ray fluorescence, absorption, and
579 diffraction. Geochimica et Cosmochimica Acta, 71, 95-128.
- 580 McCreadie, H., Jambor, J.L., Blowes, D.W., Ptacek, C., and Hiller, D. (1998)
581 Geochemical behaviour of autoclave-produced ferric arsenates and jarosite in a gold
582 mine tailings impoundment. In: Waste Characterization and Treatment. Society for
583 Mining, Metallurgy and Exploration Inc., Littleton, CO, 61-78.
- 584 Mugnaioli, E., Gorelik, T., and Kolb, U. (2009) "Ab initio" structure solution from
585 electron diffraction data obtained by a combination of automated diffraction
586 tomography and precession technique. Ultramicroscopy, 109(6), 758-765.

- 587 Paktunc, D. and Bruggeman, K. (2010) Solubility of nanocrystalline scorodite and
588 amorphous ferric arsenate: Implications for stabilization of arsenic in mine wastes.
589 Applied Geochemistry, 25, 674-683.
- 590 Paktunc, D. and Dutrizac, J.E. (2003) Characterization of arsenic substitution in synthetic
591 potassium jarosite using X-ray diffraction and X-ray absorption spectroscopy.
592 Canadian Mineralogist, 41, 905-919.
- 593 Paktunc, D., Dutrizac, J.E., and Gertsman, V. (2008) Synthesis and phase transformations
594 involving scorodite, ferric arsenate and arsenical ferrihydrite: Implications for
595 arsenic mobility. Geochimica et Cosmochimica Acta, 72, 2649-2672.
- 596 Paktunc, D., Kingston, D., Pratt, A., and McMullen, J. (2006) Distribution of gold in
597 pyrite and in products of its transformation resulting from roasting of refractory
598 gold ore. Canadian Mineralogist, 44, 213-227.
- 599 Paktunc, D., Foster, A., Heald, S., and Laflamme, G. (2004) Speciation and
600 characterization of arsenic in gold ores and cyanidation tailings using X-ray
601 absorption spectroscopy. Geochimica et Cosmochimica Acta, 68, 969-983.
- 602 Palatinus, L. and Chapuis, G. (2007) Superflip - a computer program for the solution of
603 crystal structures by charge flipping in arbitrary dimensions. Journal of Applied
604 Crystallography, 40, 786-790.
- 605 Palatinus, L. (2011) PETS - program for analysis of electron diffraction data. Institute of
606 Physics of the AS CR, Prague, Czech Republic.
- 607 Petříček, V., Dušek, M., and Palatinus, L. (2006) Jana2006. The crystallographic
608 computing system. Institute of Physics, Praha, Czech Republic.
- 609 Ravel, B. and Newville, M. (2005) ATHENA, ARTEMIS, HEPHAESTUS: data analysis
610 for X-ray absorption spectroscopy using IFEFFIT. Journal of Synchrotron
611 Radiation, 12, 537-541.
- 612 Sherman, R. and Randall, S.R. (2003) Surface complexation of arsenic(V) to iron(III)
613 (hydro)oxides: structural mechanism from ab initio molecular geometries and
614 EXAFS spectroscopy. Geochimica et Cosmochimica Acta, 67, 4223-4230.
- 615 Swash, P.M. and Monhemius, A.J. (1994) Hydrothermal precipitation from aqueous
616 solutions containing iron(III), arsenate and sulphate. Proceedings of
617 Hydrometallurgy'94, Institution of Mining and Metallurgy and the Society of

- 618 Chemical Industry, July 11-15, 1994, Cambridge, England. Chapman & Hall 176-
619 190.
- 620 Ugarte, F.J.G. and Monhemius, A.J. (1992) Characterization of high-temperature arsenic
621 containing residues from hydrometallurgical processes. *Hydrometallurgy*, 30, 69-
622 86.
- 623 USEPA (1992) Toxicity characteristics leaching procedure. Method 1311. Revised 1992,
624 35pp.
- 625 Ventruti, G., Scordari, F., Schingaro, E., Gualtieri, A., and Meneghini, C. (2005) The
626 order-disorder character of FeOHSO_4 obtained from the thermal decomposition of
627 metahohmannite, $\text{Fe}_2(\text{H}_2\text{O})_4[\text{O}(\text{SO}_4)_2]$. *American Mineralogist*, 90, 679-686.
- 628 Zabinsky, S.I., Rehr, J.J., Ankudinov, A., and Albers, R.C. (1993) FEFF 6 - Ab initio
629 Multiple-Scattering X-ray Absorption Fine Structure and X-ray Absorption Near
630 Edge Structure Code. Department of Physics, FM-15 University of Washington,
631 Seattle.

632

633 **FIGURE CAPTIONS**

634 **FIGURE 1.** Compositions of Phase 3, Phase 4, Phase 5 and Type-2 in terms of molar
635 Fe^{3+} , AsO_4 and SO_4 contents. Note that only the upper half of the plot is shown as Fe -
636 0.5AsO_4 - 0.5SO_4 . Type-2 plots are based on electron microprobe analyses. Cores are
637 represented by blue stars and exsolution-like features by purple stars (Type-2 exs).
638 Synthetic jarosite data from Paktunc and Dutrizac (2003) and scorodite from Dutrizac
639 and Jambor (1970).

640 **FIGURE 2.** XRD patterns of Phase 3, Phase 5 and Type-2. Numbers next to the patterns
641 are X_{As} mole fractions of the samples.

642 **FIGURE 3.** Polyhedral representation of the crystal structures of (a) jarosite, (b) BFS, (c)
643 scorodite, (d) $\text{FeAsO}_4 \cdot 0.75\text{H}_2\text{O}$. Fe: brown; As: purple; S: yellow; K: green.

644 **FIGURE 4.** (a) changes in unit-cell volume as a function of substitution of AsO_4 for SO_4
645 in BFS and FAS, (b) changes in the a , b and c lattice parameters of BFS (normalized to
646 $X_{\text{As}0}$ parameters) as a function of the AsO_4 fraction.

647 **FIGURE 5.** TEM photomicrographs of the FAS precipitates. The acicular crystal marked
648 04 is ferric orthoarsenate hydrate which occurs in trace amounts in the sample. The other
649 labels indicate the spots where microanalysis of the FAS crystals was performed.

650 **FIGURE 6.** Crystal structure of FAS as visualized projected along a (a) and along the
651 FeO_6 octahedral chains (b). A comparative visualization of the crystal structures of FAS
652 (c) and BFS (d), showing the rotation of the FeO_6 octahedra and AsO_4/SO_4 tetrahedra in
653 FAS. Fe: brown; As: purple; S: yellow.

654 **FIGURE 7.** (a) Backscattered electron (BSE) image and (b) X-ray maps of As and S
655 showing depletion of As along the outer margin of Type-2 grains and its enrichment in
656 exsolution-like small spotty areas or circular zones in the interior. Note that the changes
657 in S are inversely related to those of As. Scale bar of X-ray maps is 100 μm .

658 **FIGURE 8.** (a) k^3 -weighted As XAFS spectra and (b) k^3 -weighted Fe XAFS spectra of
659 BFS and FAS. Numbers next to the curves are As mole fractions: $100 \times \text{AsO}_4 / (\text{AsO}_4 + \text{SO}_4)$
660 with 0 to 12 being BFS and 34 to 75 being FAS. Experimental curves indicated by solid
661 lines and fitted spectra by circles.

662 **FIGURE 9.** (a) As and Fe concentrations (mg/L) and (b) Fe and S concentrations (mg/L)
663 in the leachates resulting from TCLP testing.

664 **FIGURE 10.** Fe^{3+} - AsO_4 - SO_4 plot showing the compositions of the pressure-oxidation
665 (POX) residues from three gold mining operations. POX-RL represents ferric arsenate-
666 sulfate grains from the Red Lake autoclave. Also shown for comparative purposes are the
667 representative mineral compositions and the synthesized compounds.

668 **FIGURE 11.** (a) k^3 -weighted As-XAFS spectra of the pressure oxidation residues from
669 the three gold mining operations and of bukovskýite. (b) k^3 -weighted Fe-XAFS spectra of
670 bukovskýite. Experimental spectra shown by solid curves and fitted spectra by circles.
671 Bukovskýite specimens from Kutna Hora (bukKH) and the Ketza River mine (bukKe).

672

673

674 **TABLE 1.** Compositions of precipitates synthesized in the Fe-AsO₄-SO₄ system
 675

Compound	Formula	Temperature (°C)	Ref.	Structure*
Type-1	Fe ₂ (HAsO ₄) ₃ ·zH ₂ O (z<4)	125-225	1	
Ferric orthoarsenate hydrate	FeAsO ₄ · ³ / ₄ H ₂ O	700-800	2	
Phase 4	Fe _{0.96} (AsO ₄) _{0.99} (SO ₄) _{0.01} (H ₂ O) _{0.54}	205-215	3	
Type-2	Fe ₄ (AsO ₄) ₃ (SO ₄) _y (OH) _x (x+2y=3)	175-225	1	FAS
Phase 3	Fe _{0.8-1.1} (AsO ₄) _{0.25-0.54} (SO ₄) _{0.46-0.75} (OH) _{0.46-0.75}	185-225	3,4	FAS
Basic iron sulfate	Fe(SO ₄)(OH)	200	5	BFS
Basic iron sulfate	Fe(SO ₄)(OH)	>175	1	BFS
Phase 5	Fe(SO ₄)(OH)	205-215	3,4	BFS
Scorodite	FeAsO ₄ ·2H ₂ O	<175	1,2,6	
Jarosite	KFe ₃ (SO ₄) ₂ (OH) ₆	98	7	

676 1: Swash and Monhemius (1994); 2: Jakeman et al. (1991); 3: Dutrizac and Jambor (2007); 4: present study;
 677 5: Johansson (1962); 6: Paktunc et al. (2008); 7: Paktunc and Dutrizac (2003); Structure*: in reference to the
 678 abbreviations used in text.
 679

680
 681

682 **TABLE 2.** Lattice parameters, space group and atomic coordinates of ferric
683 arsenate sulfate (FAS), as refined from the electron diffraction data.

684
685
686
687

Space group *I*-1

Lattice parameters: $a = 5.1639 \text{ \AA}$, $b = 5.1863 \text{ \AA}$, $c = 12.9457 \text{ \AA}$, $\alpha = 89.209^\circ$, $\beta = 89.675^\circ$, $\gamma = 87.892^\circ$,
 $V = 346.433 \text{ \AA}^3$

atom	x	y	z	U_{iso}
As/S*	0.7474(14)	0.018(2)	0.1227(6)	0.0038(18)
Fe1	0.25	-0.25	0.25	0.038(4)
Fe2	0	0.5	0	0.024(3)
O1	0.782(5)	-0.190(6)	0.0442(18)	0.026(6)
O2	0.746(5)	0.309(6)	0.083(2)	0.028(6)
O3	0.471(4)	0.014(6)	0.1906(17)	0.023(5)
O4	0.949(9)	-0.001(10)	0.208(3)	0.069(10)
OH	0.241(7)	-0.449(9)	0.123(3)	0.065(10)

688
689
690
691
692

* occupancy 50 % As, 50 % S

693
694

TABLE 3. Lattice parameters of basic ferric sulfate (BFS) and ferric arsenate-sulfate (FAS)

	<i>a</i>	<i>b</i>	<i>c</i>	α	β	γ	<i>V</i> (Å ³)
<i>BFS</i>							
XAs0	7.3434(4)	6.4133(4)	7.1330(4)				335.93(3)
XAs1	7.3353(4)	6.4143(3)	7.1377(4)				335.84(3)
XAs2	7.3357(4)	6.4145(4)	7.1359(4)				335.78(3)
XAs4	7.3431(4)	6.4178(4)	7.1393(4)				336.45(3)
XAs8	7.3565(6)	6.4215(5)	7.1407(6)				337.33(5)
XAs12	7.3936(7)	6.4261(6)	7.1414(6)				339.30(5)
Nominal(OR)	7.33	6.42	7.14				336.00
Nominal(MO)	7.33	7.14	7.39		119.7		295.27
<i>FAS</i>							
XAs26	5.1744(3)	5.1644(3)	12.9929(9)	89.641(5)	89.910(5)	87.852(4)	346.95(4)
XAs30	5.1841(5)	5.1599(5)	13.0179(12)	89.518(6)	90.022(7)	87.939(5)	347.98(5)
XAs32	5.1852(4)	5.1653(4)	13.0624(11)	89.437(4)	89.796(6)	87.837(4)	349.59(5)
XAs33	5.1801(4)	5.1674(4)	13.0483(10)	89.503(5)	89.851(5)	87.873(4)	349.02(4)
XAs34	5.1908(4)	5.1807(4)	13.0265(9)	89.599(4)	89.506(4)	87.692(4)	350.01(4)
XAs35	5.1932(3)	5.1834(4)	12.9906(11)	89.530(6)	89.460(5)	87.633(4)	349.36(4)
XAs36	5.1990(3)	5.1836(3)	12.9697(9)	89.581(4)	89.226(4)	87.590(3)	349.18(4)
XAs37.1	5.2018(6)	5.1744(6)	13.091(2)	89.321(6)	90.15(1)	88.044(7)	352.14(7)
XAs37.3	5.1835(3)	5.1739(3)	13.0515(8)	89.415(4)	89.818(4)	87.830(3)	349.76(3)
XAs38	5.2082(6)	5.1721(6)	13.095(2)	89.409(6)	89.920(9)	87.999(7)	352.50(7)
XAs40	5.1985(3)	5.1764(3)	13.1062(8)	89.427(4)	89.775(4)	87.870(3)	352.42(4)
XAs42	5.1939(4)	5.1649(4)	13.1357(13)	89.267(5)	89.679(6)	87.771(5)	352.07(5)
XAs44	5.2131(3)	5.2051(3)	13.0583(9)	89.556(4)	89.208(4)	87.544(3)	353.97(4)
XAs45	5.2042(3)	5.1815(3)	13.0774(8)	89.600(4)	89.911(4)	87.996(3)	352.41(4)
XAs46	5.2068(4)	5.1854(4)	13.0626(10)	89.615(5)	89.913(5)	88.023(5)	352.46(5)
XAs46.6	5.2147(3)	5.1934(3)	13.0690(8)	89.621(4)	89.909(4)	88.129(4)	353.74(4)
XAs47	5.2192(3)	5.1956(4)	13.1330(10)	89.366(4)	89.755(4)	87.861(4)	355.85(4)
XAs48	5.2264(5)	5.1979(4)	13.1119(12)	89.550(6)	89.924(6)	88.040(5)	355.98(5)
XAs51.3	5.2341(3)	5.2140(4)	13.0527(9)	89.564(5)	90.048(4)	88.340(4)	356.05(4)
XAs51.6	5.2293(4)	5.1974(4)	13.1172(12)	89.487(5)	89.929(6)	88.122(5)	356.31(5)
XAs51.8	5.2319(4)	5.2142(4)	13.0881(10)	89.731(6)	89.952(6)	88.186(4)	356.86(5)
XAs52.0	5.2124(3)	5.1960(4)	13.1187(9)	89.464(5)	89.621(5)	87.835(5)	355.03(4)
XAs52.1	5.2059(5)	5.1849(4)	13.1244(11)	89.381(5)	89.679(6)	87.760(5)	353.96(5)
XAs52.2	5.2219(3)	5.1946(4)	13.1404(9)	89.408(4)	89.809(4)	87.930(4)	356.19(4)
XAs52.3	5.2118(5)	5.1898(5)	13.1267(12)	89.386(6)	89.721(6)	87.788(5)	354.77(6)
XAs59	5.2187(4)	5.2397(4)	13.0298(11)	89.578(6)	88.938(5)	87.888(5)	355.98(5)
XAs62	5.2173(4)	5.2506(3)	13.0150(10)	89.558(5)	88.900(5)	88.168(5)	356.28(4)
XAs63	5.2225(3)	5.20014(33)	13.1390(8)	89.435(4)	89.779(4)	87.854(4)	356.55(4)
XAs75	5.2134(4)	5.2415(4)	13.0156(12)	89.519(6)	88.837(5)	87.781(5)	355.31(5)
<i>Scorodite</i>							

XAs84	8.9365(3)	10.2617(4)	10.0553(4)	922.11(6)
XAs92±3	8.9394(6)	10.2871(6)	10.0435(6)	923.61(9)
XAs93	8.9335(8)	10.2610(8)	10.0484(8)	921.1(1)
XAs99	8.9514(9)	10.3254(10)	10.0369(9)	927.7(1)
Nominal*	8.937(1)	10.278(2)	9.996(2)	918.2(3)

695 Nominal FeOH₂SO₄ lattice parameters (OR) from Johannson (1962) and (MO) from Ventruti et al. (2005);

696 Nominal scorodite is based on Hawthorne (1976); Numbers in sample labels next to XAs refer to

697 100×AsO₄/(AsO₄+SO₄); *a*, *b* and *c* in Å; *α*, *β* and *γ* in degrees; numbers in bracket are uncertainty values.

698

699

700

701

702

703

704

705
706
707

TABLE 4. Arsenic XAFS fitting results

Sample		<i>N</i>	<i>R</i>	σ^2	<i>E0</i>	<i>rf</i>	<i>Ni/Nv</i>
XAs8	O	4*	1.68±0.01	0.0008	-0.9	0.033	1.7
	Fe	4*	3.34±0.02	0.0074			
	S	3.5*	3.72±0.02	0.0047			
	MS2-1	12*	3.08±0.12	0.0085			
XAs12	O	4*	1.68±0.01	0.0009	0.4	0.029	1.7
	Fe	4*	3.35±0.02	0.0087			
	S	3.5*	3.73±0.02	0.0046			
	MS2-1	12*	3.07±0.09	0.0044			
XAs34	O	4*	1.68±0.01	0.0020	0.5	0.017	1.5
	Fe	4*	3.34±0.02	0.0111			
	S	2.6*	3.72±0.03	0.0064			
	As	1.4*	4.01±0.05	0.0085			
	MS2-1	12*	3.14±0.08	0.0127			
XAs35	O	4*	1.69±0.01	0.0012	2.0	0.012	1.5
	Fe	4*	3.38±0.02	0.0108			
	S	2.6*	3.76±0.02	0.0028			
	As	1.4*	4.06±0.02	0.0043			
	MS2-1	12*	3.11±0.07	0.0040			
XAs37	O	4*	1.68±0.01	0.0010	-0.2	0.016	1.5
	Fe	4*	3.35±0.02	0.0091			
	S	2.5*	3.73±0.03	0.0038			
	As	1.5*	4.02±0.04	0.0064			
	MS2-1	12*	3.11±0.11	0.0079			
XAs47	O	4*	1.69±0.01	0.0014	1.4	0.009	1.5
	Fe	4*	3.39±0.03	0.0123			
	S	2*	3.76±0.03	0.0024			
	As	2*	4.07±0.04	0.0084			
	MS2-1	12*	3.12±0.09	0.0060			
XAs59	O	4*	1.68±0.01	0.0012	-0.5	0.015	1.5
	Fe	4*	3.35±0.02	0.0103			
	S	1.6*	3.70±0.03	0.0011			
	As	2.4*	4.02±0.06	0.0115			
	MS2-1	12*	3.15±0.18	0.0017			
XAs63	O	4*	1.68±0.01	0.0013	1.4	0.011	1.5
	Fe	4*	3.38±0.03	0.0045			
	S	1.5*	3.74±0.02	0.0015			
	As	2.5*	4.05±0.03	0.0089			
	MS2-1	12*	3.10±0.07	0.0045			
XAs75	O	4*	1.68±0.01	0.0014	-0.4	0.015	1.7
	Fe	4*	3.38±0.03	0.0151			
	As	3*	3.99±0.07	0.0155			
	MS2-1	12*	3.10±0.08	0.0039			

708 Fit performed in *k*-space (3-13 Å⁻¹); amplitude reduction factor (*S*₀²) is constrained to 0.9 following its
 709 optimization; *N*: coordination number; *R*: interatomic distance (Å); σ^2 : Debye-Waller parameter (Å²); *E0*:
 710 energy offset (eV); *rf*: r-factor as goodness-of-fit; *Ni/Nv*: number of independent points/number of variables;
 711 * Fixed value; Multiple scattering paths, MS2-1, MS3-1 and MS3-2 refer to As-O1-O2, As-O1-As-O2 and
 712 As-O1-As-O1, respectively (Manceau et al. 2007); *N* and *R* values of MS3-1 and MS3-2 were fixed to their
 713 crystallographic values (i.e. 12 at 3.34 Å and 4 at 3.34 Å, respectively) and their Debye-Waller parameters
 714 were constrained to be identical with that of MS2-1; Numbers in sample labels next to XAs refer to
 715 100×AsO₄/(AsO₄+SO₄).
 716

717
 718
 719

TABLE 5. Iron XAFS fitting results

Sample		<i>N</i>	<i>R</i>	σ^2	<i>E0</i>	<i>rf</i>
XAs0	O	6*	2.00±0.01	0.0054	-0.3	0.017
	S	4*	3.38±0.02	0.0111		
	Fe1	2*	3.69±0.03	0.0122		
	Fe2	8*	5.12±0.02	0.0122 ^a		
XAs8	O	6*	1.99±0.01	0.0062	-2.3	0.025
	S	3.7*	3.38±0.03	0.0147		
	Fe1	2*	3.69±0.03	0.0132		
	Fe2	8*	5.12±0.02	0.0132 ^a		
XAs12	O	6*	1.99±0.01	0.0076	-3.6	0.039
	S	3.5*	3.34±0.03	0.0174		
	Fe1	2*	3.71±0.05	0.0163		
	Fe2	8*	5.10±0.03	0.0163 ^a		
XAs34	O	6*	1.97±0.01	0.0094	0.6	0.027
	As	1.4*	3.32±0.06	0.0145		
	Fe1	2*	3.68±0.04	0.0193		
	Fe2	8*	5.14±0.04	0.0193 ^a		
XAs35	O	6*	1.97±0.01	0.0093	0.8	0.026
	As	1.4*	3.32±0.04	0.0155		
	Fe1	2*	3.67±0.06	0.0200		
	Fe2	8*	5.14±0.04	0.0200 ^a		
XAs47	O	6*	1.96±0.01	0.0106	0.9	0.027
	As	2*	3.31±0.02	0.0117		
	Fe1	2*	3.62±0.06	0.0201		
	Fe2	8*	5.18±0.04	0.0201 ^a		
XAs62	O	6*	1.96±0.01	0.0111	0.8	0.031
	As	2.5*	3.32±0.02	0.0112		
	Fe1	2*	3.62±0.10	0.0241		
	Fe2	8*	5.17±0.06	0.0241 ^a		
XAs75	O	6*	1.97±0.01	0.0110	2.6	0.029
	As	3*	3.34±0.02	0.0140		
	Fe1	2*	3.65±0.08	0.0213		
	Fe2	8*	5.17±0.04	0.0213 ^a		

720 Fit performed in *k*-space (2.5-12 Å⁻¹); amplitude reduction factor (*S*₀²) is constrained to 0.9 following its
 721 optimization; *N*: coordination number; *R*: interatomic distance (Å); σ^2 : Debye–Waller parameter (Å²); *E0*:
 722 energy offset (eV); *rf*: r-factor as goodness-of-fit; number of independent points/number of variables=2 for
 723 all; * Fixed value optimized to crystallographic value; ^a: constrained to be identical with preceding Debye–
 724 Waller parameter. Numbers in sample labels next to XAs refer to 100×AsO₄/(AsO₄+SO₄).

725
 726
 727

728 **TABLE 6.** Arsenic XAFS fitting of pressure oxidation residues and bukovskýite
 729

		<i>N</i>	<i>R</i>	σ^2	<i>E0</i>	<i>rf</i>	<i>Ni/Nv</i>
POX-2	O	4*	1.68±0.01	0.0013	6.2	0.013	1.5
	Fe	4*	3.38±0.03	0.0129			
	S	2*	3.72±0.04	0.0055			
	As	2*	4.05±0.05	0.0097			
	MS2-1	12*	3.11±0.09	0.0081			
POX-9	O	4*	1.70±0.01	0.0019	7.8	0.032	1.6
	Fe	2*	3.43±0.04	0.0086			
	MS2-1	12*	3.13±0.07	0.0009			
POX-14	O	4*	1.69±0.01	0.0016	5.8	0.020	1.6
	Fe	2*	3.35±0.05	0.0133			
	MS2-1	12*	3.11±0.06	0.0010			
bukKH	O	4*	1.69±0.01	0.0014	5.8	0.011	1.7
	Fe	4*	3.36±0.02	0.0092			
	As	2*	3.95±0.06	0.0113			
	MS2-1	12*	3.10±0.07	0.0034			
bukKe	O	4*	1.69±0.01	0.0011	6.3	0.011	1.7
	Fe	4*	3.35±0.01	0.0077			
	As	2*	3.95±0.05	0.0113			
	MS2-1	12*	3.13±0.07	0.0045			

730 Fit performed in *k*-space (3–13 Å⁻¹); amplitude reduction factor (*S*₀²) is constrained to 0.9 following its
 731 optimization; *N*: coordination number; *R*: interatomic distance (Å); σ^2 : Debye–Waller parameter (Å²); *E0*:
 732 energy offset (eV); *rf*: r-factor as goodness-of-fit; Multiple scattering paths, MS2-1, MS3-1 and MS3-2 refer to
 733 As–O1–O2, As–O1–As–O2 and As–O1–As–O1, respectively (Manceau et al. 2007); * Fixed value; *N* and *R*
 734 values of MS3-1 and MS3-2 were fixed to their crystallographic values (i.e. 12 at 3.34 Å and 4 at 3.34 Å,
 735 respectively) and their Debye-Waller parameters were constrained to be identical with MS2-1; bukKH:
 736 bukovskýite from Kutna Hora, Czech Republic; bukKe: bukovskýite from Ketz River Mine, Yukon, Canada;
 737 POX-2, -9, -14 pressure oxidation residues from gold processing operations.

738

739

740

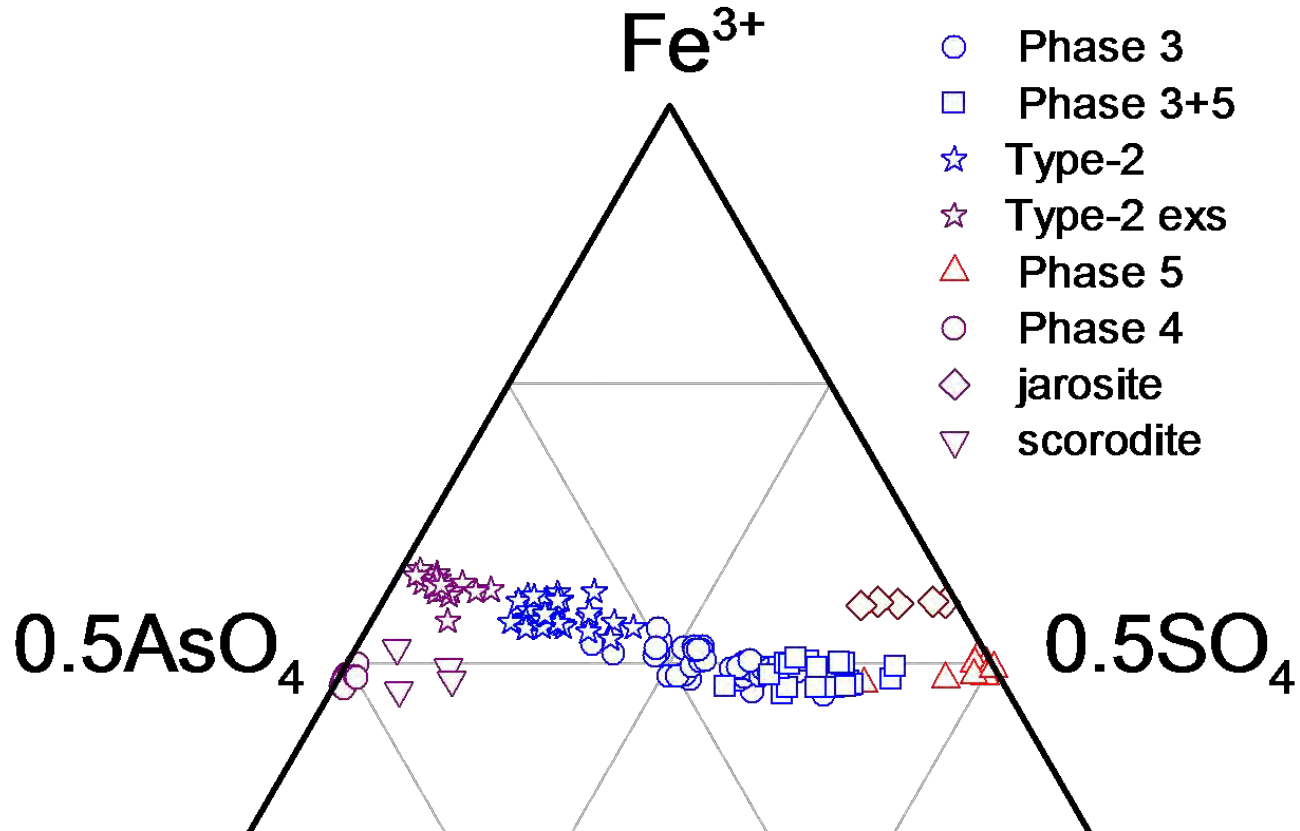
741 **TABLE 7.** Fe-XAFS fitting of bukovskýite
 742

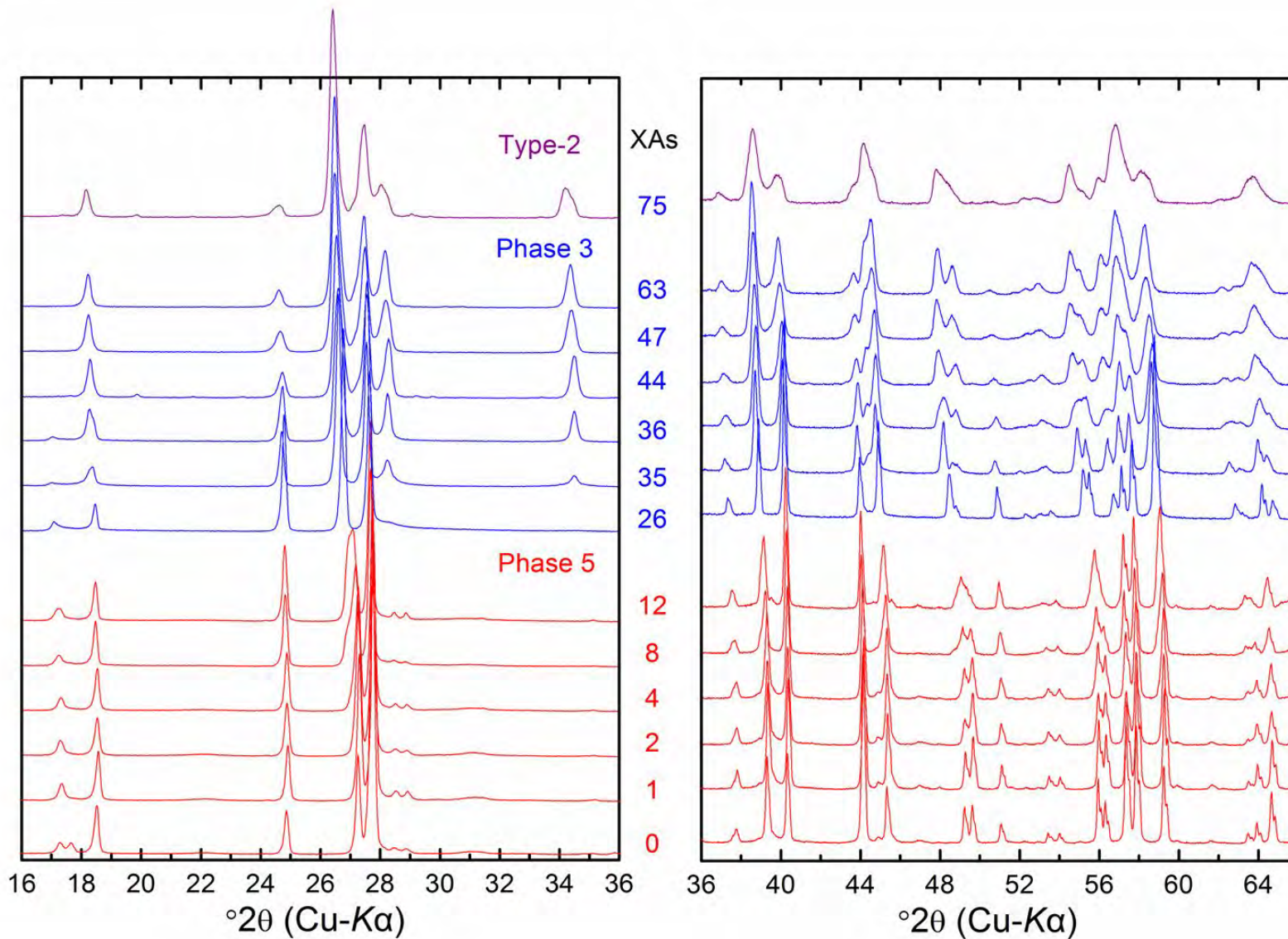
		<i>N</i>	<i>R</i>	σ^2	<i>rf</i>	<i>E0</i>
bukKH	O	6*	1.99±0.01	0.0084	0.029	-3.5
	As	2*	3.35±0.01	0.0076		
	Fe1	1*	3.62±0.02	0.0064		
	Fe2	1*	5.08±0.04	0.0064 ^a		
bukKe	O	6*	1.99±0.01	0.0079	0.033	-4.4
	As	2*	3.34±0.01	0.0057		
	Fe1	1*	3.60±0.02	0.0058		
	Fe2	1*	5.09±0.04	0.0058 ^a		

743 Fit performed in *k*-space (3–13 Å⁻¹); amplitude reduction factor (*S*₀²) is constrained to 0.9 following its
 744 optimization; *N*: coordination number; *R*: interatomic distance (Å); σ^2 : Debye–Waller parameter (Å²); *E0*:
 745 energy offset (eV); *rf*: r-factor as goodness-of-fit; number of independent points/number of variables=2;
 746 *: Fixed value optimized to crystallographic value; ^a: constrained to be identical with preceding Debye–Waller
 747 parameter. bukKH: bukovskýite from Kutna Hora, Czech Republic; bukKe: bukovskýite from Ketz River
 748 Mine, Yukon, Canada.

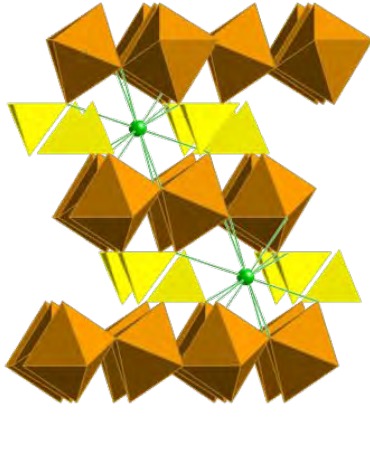
749

750

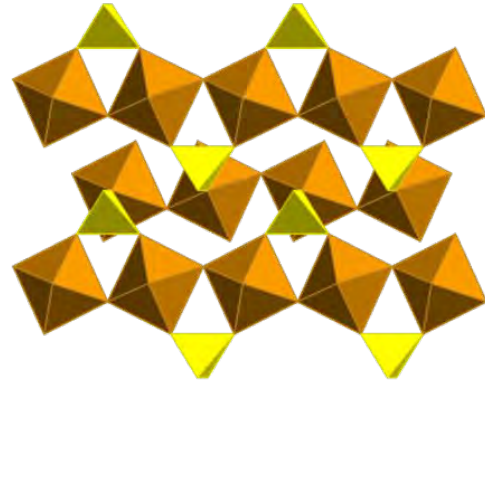




a



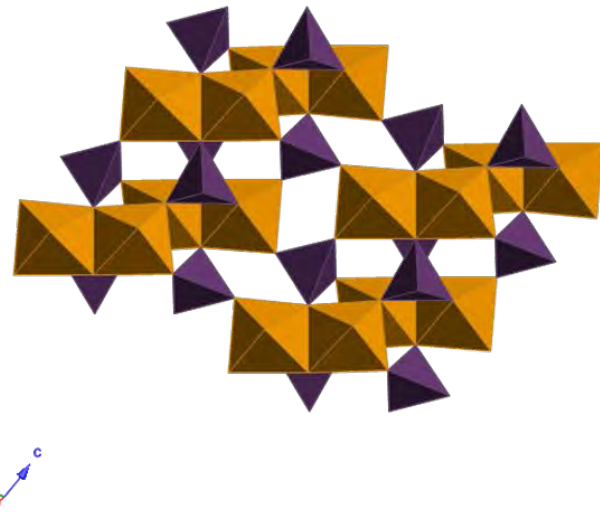
b

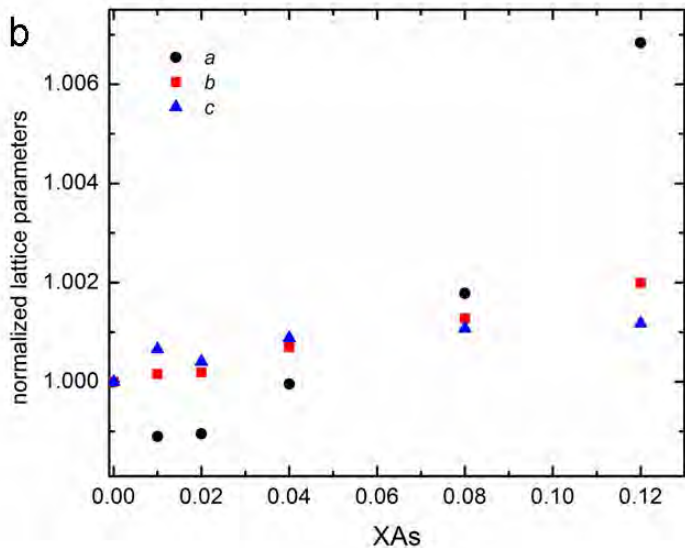
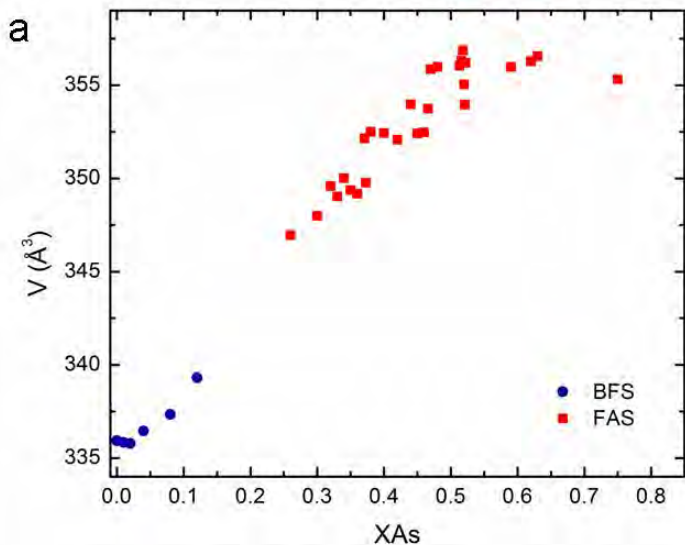


c

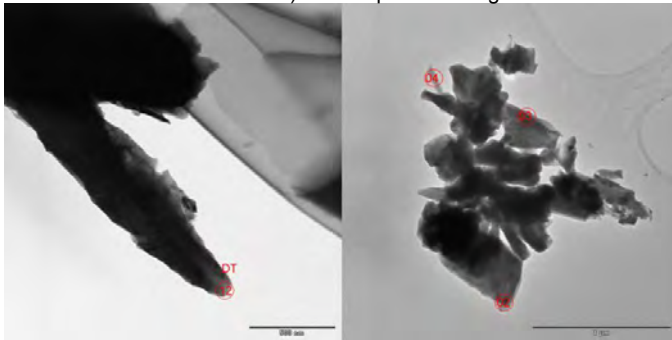


d



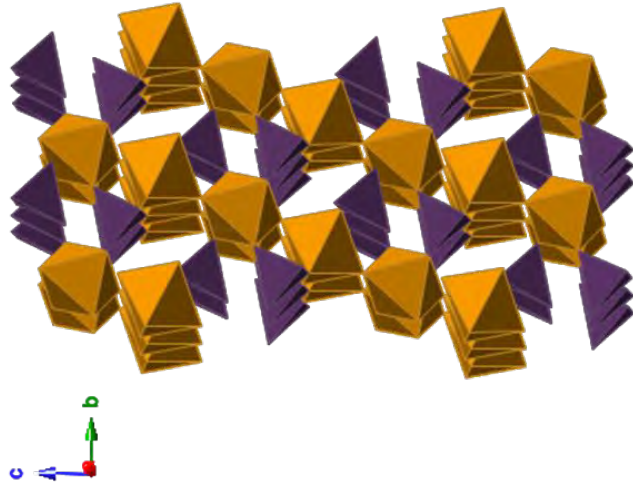


This is a preprint, the final version is subject to change, of the American Mineralogist (MSA)
Cite as Authors (Year) Title. American Mineralogist, in press.
(DOI will not work until issue is live.) DOI: <http://dx.doi.org/10.2138/am.2013.4342>

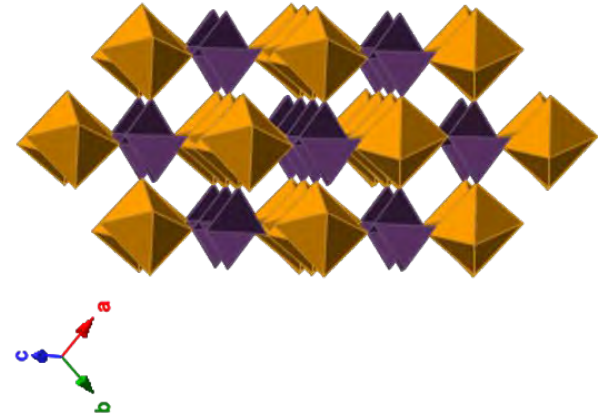


Always consult and cite the final, published document. See <http://www.minsocam.org> or GeoscienceWorld

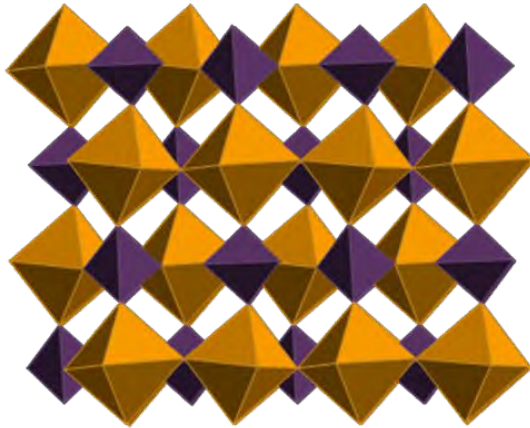
a



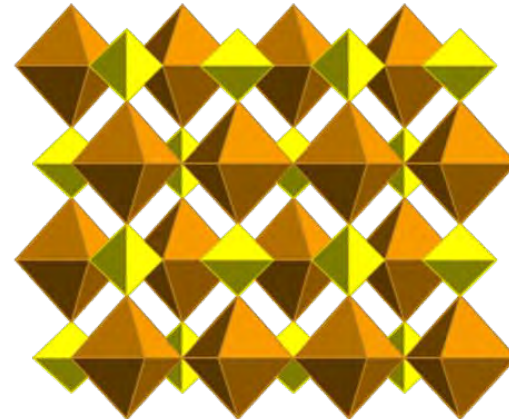
b

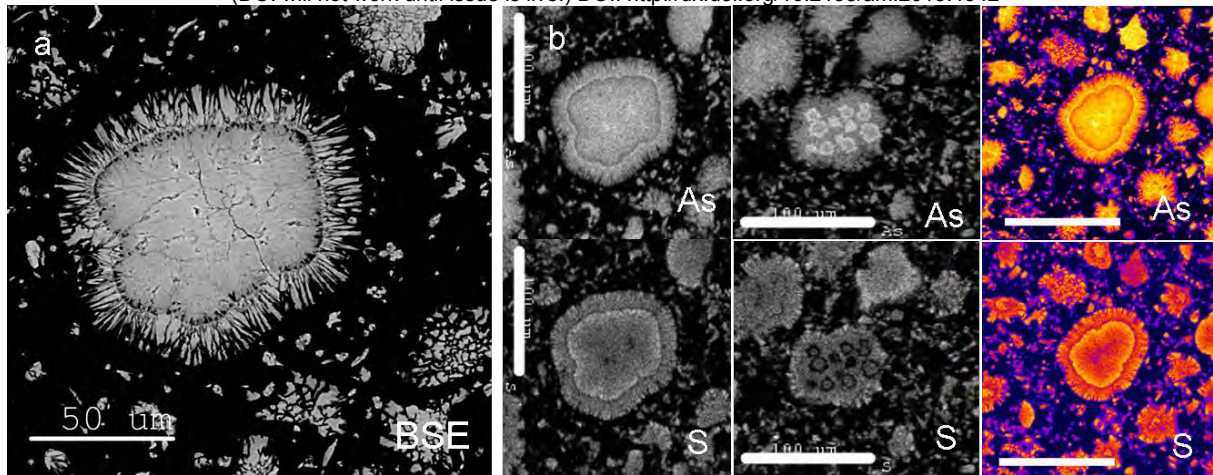


c

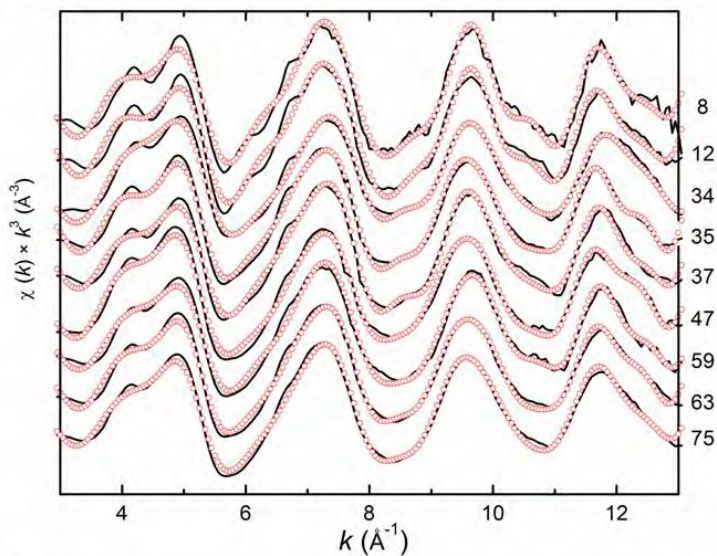


d





a



b

